Effects of Viscous Anisotropy on Pipe Poiseuille Flow

Jane Allwright and Richard Katz

November 21, 2013

1 Introduction

Regions of partially molten rock in the Earth's mantle are of interest to Earth scientists, being key to understanding and predicting volcanism and the development of the mantle. Observations and experiments must be carried out in laboratories, while theory and models are also studied and developed to better match and explain the observations. In this article we consider a low-porosity system in which magma flows in the pores in a matrix of solid grains. The system at the grain-scale is important in explaining the model of an anisotropic viscosity [Takei and Holtzman, 2009a,b,c, Katz and Takei, 2013a] but, by averaging over a representative volume element [Katz and Spiegelman, 2012], the system is considered a continuum for the purposes of the equations.

In the model of viscous anisotropy, which was developed by Takei and Holtzman [2009a,b,c] using experimental evidence from Daines and Kohlstedt [1997] and Zimmerman et al. [1999], and which has been studied by Butler [2012] and Katz and Takei [2013a,b], we consider a matrix of solid grains with liquid magma flowing in channels between the grains. The porosity is assumed to be small: Takei and Holtzman [2009c] consider ϕ lying between about 0.02 and 0.189; Butler [2012] uses an initial value of $\phi_0 = 0.01$ and allows $0 \leq \phi \leq 0.02$; and Katz and Takei [2013a,b] consider $\phi_0 = 0.05$ and $\phi \leq 0.2$. Anisotropy, caused by a reduced contact area between grains, develops in the direction of the largest principal stress, leading to a direction-dependent viscosity [Takei and Holtzman, 2009a].

There has been experimental work on simple shear and torsion, investigated by Holtzman et al. [2003] and King et al. [2010]. Katz and Takei investigated the theory of these configurations using the model of anisotropic viscosity, and presented a qualitative explanation of some of the observations [Katz and Takei, 2013a,b]. Katz and Takei also considered planar Poiseuille flow between two parallel plates. Here, we investigate gravity-driven Poiseuille flow in a cylindrical pipe, employing the same anisotropy model used by Katz and Takei. This will build on their work and will be more suited for comparison with new experiments which are being undertaken in pipe Poiseuille geometry.

In this article we recall the equations governing the system, which we study first under the (problematic) simplification of uniform anisotropy and later in their full, non-linear, form. In our work, we discuss the problems associated with the model of uniform anisotropy, and propose a non-uniform approximation to the anisotropy parameters. Using such an approximation, we still need only solve *linear* differential equations for the velocity, but we obtain results very close to the numerical solution of the full problem at $t = 0$. The finite time, numerical solutions form the final part of our theoretical investigation.

The results, and comparison with observations, will give more information to theorists regarding where the current model works and where it fails, and enable further refinement of the model to better fit experimental results.

2 Governing Equations

2.1 Equations

The governing equations are derived from the conservation of mass and the force balance on each of the two phases. Combining these, and assuming zero melting rate, the system can be written in terms of the following variables:

ϕ	porosity
$\mathbf{v^S}$	solid velocity
K	permeability (dependent on porosity)
η_L	liquid viscosity
p^L	liquid pressure
ρ_L, ρ	liquid density, phase-averaged density (assumed to be equal).

Letting e_{kl} be the strain-rate tensor of the solid phase, the governing equations can be written in the following form [Katz and Takei, 2013a, Takei and Holtzman, 2009c, Katz and Spiegelman, 2012, Rudge et al., 2010]:

$$\frac{\partial \phi}{\partial t} = \nabla \cdot ((1-\phi)\mathbf{v}^{\mathbf{S}}), \tag{1}$$

$$\nabla \cdot \mathbf{v}^{\mathbf{S}} = \nabla \cdot \left(\frac{K}{\eta_L} (\nabla p^L - \rho_L \mathbf{g}) \right), \tag{2}$$

$$\partial_i p^L = \partial_j (\sigma_{ij} + p^L \delta_{ij}) + \rho g_i, \tag{3}$$

$$\sigma_{ij} + p^L \delta_{ij} = c_{ijkl} e_{kl}. \tag{4}$$

The fourth-rank tensor c_{ijkl} is the viscosity tensor, which in this case will incorporate the anisotropy into the system. The explicit form of c_{ijkl} is given below, in equation (17).

In cylindrical polar coordinates (r, θ, z) defined so that $\mathbf{g} = -g\hat{\mathbf{z}}$, and the axis of the cylinder lies along the z-axis, equations (1), (2) and (3) become:

$$\frac{\partial \phi}{\partial t} = \frac{1}{r}\frac{\partial}{\partial r}(r(1-\phi)v_r) + \frac{1}{r}\frac{\partial}{\partial \theta}((1-\phi)v_\theta) + \frac{\partial}{\partial z}((1-\phi)v_z), \tag{5}$$

$$\frac{1}{r}\frac{\partial}{\partial r}(rv_r) + \frac{1}{r}\frac{\partial v_\theta}{\partial \theta} + \frac{\partial v_z}{\partial z} = \frac{1}{r}\frac{\partial}{\partial r}\left(\frac{Kr}{\eta_L}\frac{\partial p^L}{\partial r}\right) + \frac{1}{r}\frac{\partial}{\partial \theta}\left(\frac{K}{\eta_L r}\frac{\partial p^L}{\partial \theta}\right) + \frac{\partial}{\partial z}\left(\frac{K}{\eta_L}\left(\frac{\partial p^L}{\partial z} + \rho_L g\right)\right), \tag{6}$$

$$\frac{\partial p^L}{\partial r} = \frac{\partial}{\partial r}(\sigma_{rr} + p^L) + \frac{1}{r}\frac{\partial}{\partial \theta}\sigma_{r\theta} + \frac{\sigma_{rr} - \sigma_{\theta\theta}}{r} + \frac{\partial}{\partial z}\sigma_{rz}, \tag{7}$$

$$\frac{1}{r}\frac{\partial p^L}{\partial \theta} = \frac{\partial}{\partial r}\sigma_{r\theta} + \frac{1}{r}\frac{\partial}{\partial \theta}(\sigma_{\theta\theta} + p^L) + \frac{2\sigma_{r\theta}}{r} + \frac{\partial}{\partial z}\sigma_{\theta z}, \tag{8}$$

$$\frac{\partial p^L}{\partial z} = \frac{\partial}{\partial r}\sigma_{rz} + \frac{1}{r}\frac{\partial}{\partial \theta}\sigma_{\theta z} + \frac{\sigma_{rz}}{r} + \frac{\partial}{\partial z}(\sigma_{zz} + p^L) - \rho g. \tag{9}$$

We consider only axisymmetric cases, where $\frac{\partial v_r}{\partial \theta} = \frac{\partial v_z}{\partial \theta} = \frac{\partial p^L}{\partial \theta} = \frac{\partial \phi}{\partial \theta} = 0$, and in which $v_\theta = 0$. Using the notation of Katz and Takei [2013a,b], we assume the maximal principal stress, σ_3, is in the r-z plane, at an angle Θ to the z axis, and let α be the magnitude of anisotropy. It will be useful throughout this article to define

$$A = r_\xi - \frac{2}{3} - \alpha \cos^2\Theta \sin^2\Theta, \tag{10}$$

$$B = r_\xi + \frac{4}{3} - \alpha \sin^4\Theta, \tag{11}$$

$$C = r_\xi - \frac{2}{3}, \tag{12}$$

$$D = \alpha \cos\Theta \sin^3\Theta, \tag{13}$$

$$E = \alpha \cos^3\Theta \sin\Theta, \tag{14}$$

$$F = r_\xi + \frac{4}{3} - \alpha \cos^4\Theta, \tag{15}$$

where, r_ξ is the bulk/shear viscosity ratio, taken to be a constant of about $\frac{5}{3}$ [Katz and Takei, 2013a].

With these assumptions, e_{ij} is given as

$$(e_{ij}) = \begin{array}{c} \\ z \\ r \\ \theta \end{array} \begin{array}{c} \begin{array}{ccc} z & r & \theta \end{array} \\ \begin{pmatrix} \frac{\partial v_z}{\partial z} & \frac{1}{2}\left(\frac{\partial v_z}{\partial r} + \frac{\partial v_r}{\partial z}\right) & 0 \\ \frac{1}{2}\left(\frac{\partial v_z}{\partial r} + \frac{\partial v_r}{\partial z}\right) & \frac{\partial v_r}{\partial r} & 0 \\ 0 & 0 & \frac{v_r}{r} \end{pmatrix} \end{array} \tag{16}$$

and the viscosity tensor (using the model in Katz and Takei [2013a,b]) has components

$$(c_{ijkl}) = \eta_0 e^{-\lambda(\phi-\phi_0)} \times \begin{array}{c} \\ zz \\ rr \\ \theta\theta \\ r\theta \\ \theta z \\ zr \end{array} \begin{array}{c} \begin{array}{cccccc} zz & rr & \theta\theta & r\theta & \theta z & zr \end{array} \\ \begin{pmatrix} F & A & C & 0 & 0 & -E \\ A & B & C & 0 & 0 & -D \\ C & C & C+2 & 0 & 0 & 0 \\ 0 & 0 & 0 & 1 & 0 & 0 \\ 0 & 0 & 0 & 0 & 1 & 0 \\ -E & -D & 0 & 0 & 0 & A-C+1 \end{pmatrix} \end{array}, \tag{17}$$

where λ is a constant, typically taken in the range 25–27 [Takei and Holtzman, 2009c, Katz and Takei, 2013a], and the remaining components of the fourth-rank tensor c_{ijkl} follow by symmetry.

Finally, a relation must be specified between the permeability K and porosity ϕ. For small porosity, as considered here, K is typically assumed to be proportional to ϕ^n, with $n \approx 1$–3 [D.McKenzie, 1989, Riley and Kohlstedt, 1991, Faul, 1997, Wark and Watson, 1998].

2.2 Scaling and non-dimensionalisation

Let H be the radius of the cylinder, and let $U = \dfrac{\rho g H^2}{\eta_0}$ (giving a typical order of magnitude of a velocity through the pipe). Then we introduce rescaled, dimensionless variables as follows:

$$\begin{aligned}
&\mathbf{X} = \frac{\mathbf{x}}{H}, && \mathbf{V} = \frac{\mathbf{v}^{\mathbf{S}}}{U}, && K^* = \frac{K}{K_0} = \left(\frac{\phi}{\phi_0}\right)^n,\\
&\sigma^*_{ij} = \frac{\sigma_{ij} + p^L\delta_{ij}}{\left(\dfrac{\eta_0 U}{H}\right)}, && P = \frac{p^L}{\rho g H}, && e^*_{ij} = \frac{e_{ij}}{\left(\frac{U}{H}\right)},\\
&c^*_{ijkl} = \frac{c_{ijkl}}{\eta_0}, && \tau = \frac{t}{\left(\dfrac{H}{U}\right)}. &&
\end{aligned}$$

For the remainder of this article we shall use the variables r and z to denote the dimensionless radial and vertical coordinates.

We also define the non-dimensionalised compaction length, R, by $R = \dfrac{1}{H}\sqrt{\dfrac{(r_\xi + \frac{4}{3})\eta_0 K_0}{\eta_L}}$. This is a key parameter, depending on the material properties of the solid and liquid phases. If the porosity is initially constant, R defines the radial distance from the boundary over which matrix compaction is expected to occur [McKenzie, 1984].

Substituting the non-dimensional variables into the governing equations, and using the above assumptions, we get the non-dimensionalised system:

$$\frac{\partial \phi}{\partial \tau} = \nabla \cdot ((1-\phi)\mathbf{V}), \tag{18}$$

$$\nabla \cdot \mathbf{V} = \frac{R^2}{r_\xi + \frac{4}{3}} \nabla \cdot (K^*(\nabla P + \hat{\mathbf{z}})), \tag{19}$$

$$\frac{\partial P}{\partial r} = \frac{\partial}{\partial r}\sigma^*_{rr} + \frac{\sigma^*_{rr} - \sigma^*_{\theta\theta}}{r} + \frac{\partial}{\partial z}\sigma^*_{rz}, \tag{20}$$

$$\frac{\partial P}{\partial z} = \frac{\partial}{\partial r}\sigma^*_{rz} + \frac{\partial}{\partial z}\sigma^*_{zz} + \frac{\sigma^*_{rz}}{r} - 1, \tag{21}$$

where

$$\sigma^*_{zz} = e^{-\lambda(\phi-\phi_0)} \times \left[F\frac{\partial V_z}{\partial z} + A\frac{\partial V_r}{\partial r} + C\frac{V_r}{r} - E\left(\frac{\partial V_z}{\partial r} + \frac{\partial V_r}{\partial z}\right)\right], \tag{22}$$

$$\sigma^*_{rr} = e^{-\lambda(\phi-\phi_0)} \times \left[A\frac{\partial V_z}{\partial z} + B\frac{\partial V_r}{\partial r} + C\frac{V_r}{r} - D\left(\frac{\partial V_z}{\partial r} + \frac{\partial V_r}{\partial z}\right)\right], \tag{23}$$

$$\sigma^*_{\theta\theta} = e^{-\lambda(\phi-\phi_0)} \times \left[C\frac{\partial V_z}{\partial z} + C\frac{\partial V_r}{\partial r} + (C+2)\frac{V_r}{r}\right], \tag{24}$$

$$\sigma^*_{rz} = e^{-\lambda(\phi-\phi_0)} \times \left[-E\frac{\partial V_z}{\partial z} - D\frac{\partial V_r}{\partial r} + (A - C + 1)\left(\frac{\partial V_z}{\partial r} + \frac{\partial V_r}{\partial z}\right)\right]. \tag{25}$$

2.3 Boundary conditions

The boundary conditions are $V_r = V_z = 0$ at $r = 1$. We also require that the solution is non-singular at the centre line $r = 0$, and expect that this will lead to the symmetry conditions $V_r = \dfrac{\partial V_z}{\partial r} = \dfrac{\partial P}{\partial r} = 0$ at $r = 0$.

We make the mathematical assumption of an infinitely long pipe. This means that for the unperturbed (base state) solution, we have $\dfrac{\partial V_r}{\partial z} = \dfrac{\partial V_z}{\partial z} = \dfrac{\partial P}{\partial z} = 0$.

As a final boundary condition, since the pressure was only defined up to an additive constant, we choose (without loss of generality) that $P = 0$ at $r = 0$.

2.4 The 'base state and perturbations' approach

Using the terminology of Katz and Takei [2013a,b] for an approach also used by Takei and Holtzman [2009c] and Butler [2012], we consider first the 'base state' solution (with index 0), which will be the z-independent solution to the system of equations with an initially uniform porosity, ϕ_0, and then we consider the response of the system to small perturbations in the initial porosity, of order $\varepsilon \ll 1$:

$$\phi = \phi_0 + \varepsilon\phi_1 + O(\varepsilon^2), \tag{26}$$

$$P = P_0 + \varepsilon P_1 + O(\varepsilon^2), \tag{27}$$

$$\mathbf{V} = \mathbf{V^0} + \varepsilon\mathbf{V^1} + O(\varepsilon^2). \tag{28}$$

We also define the 'compaction rate' by $\mathcal{C} \equiv \nabla \cdot \mathbf{V}$, and write

$$\mathcal{C} = \mathcal{C}_0 + \varepsilon\mathcal{C}_1 + O(\varepsilon^2). \tag{29}$$

For the base state at $\tau = 0$, equations (19) and (20) can be combined, and equations (19) and (21) can be integrated. Applying the condition that there is no singularity at $r = 0$, we find that the initial base state solution must satisfy

$$-D\frac{\partial V_r}{\partial r} + (A - C + 1)\frac{\partial V_z}{\partial r} = \frac{r}{2} \tag{30}$$

and

$$V_r = \frac{R^2}{r_\xi + \frac{4}{3}}\left[\left(B - \frac{D^2}{A - C + 1}\right)\left(\frac{\partial^2 V_r}{\partial r^2} + \frac{1}{r}\frac{\partial V_r}{\partial r}\right) - (C + 2)\frac{V_r}{r^2} - \frac{D}{A - C + 1}\right]. \tag{31}$$

3 Uniform anisotropy analysis

3.1 The uniform anisotropy model

For an anisotropic viscosity, we have non-zero anisotropy parameters, Θ and α. These will vary with position, and satisfy the symmetry conditions $\dfrac{\partial\alpha}{\partial r} = 0$ and $\Theta = 0$ at $r = 0$. (In fact Θ should be an odd function of r, and α should be an even function.) However, following the pattern of Katz and Takei [2013a], in this section we consider imposing constant and non-zero Θ and α. This is a simplified case of viscous anisotropy, intended to give a first comparison of the isotropic and the anisotropic system. This section will allow a full comparison of the 2D Poiseuille results of Katz and Takei with this cylindrical Poiseuille flow.

We expect difficulties at $r = 0$, where a non-zero Θ will prevent the equations, and the solution, from being smooth. The results of this section are not, therefore, being presented as a possible solution, but as a first step into the model of viscous anisotropy and a means of comparison with the work of Katz and Takei. Solving the equations under this approximation is a step which can be tackled analytically, and one for which we have an explicit mathematical formula for the solution, in addition to the numerical results. This lets us understand *exactly* the manner in which the solutions fail at $r = 0$, and makes it clear that a better model is required.

3.2 Base state solution at $\tau = 0$

With constant anisotropy, equation (31), after a suitable transformation, is a forced modified Bessel equation of order $\nu = \sqrt{\dfrac{C + 2}{B - \frac{D^2}{A-C+1}}}$. The solution which satisfies the boudary condition at $r = 1$ and is finite at $r = 0$ is given explicitly as

$$V_r^0(r) = V_p(r) - \frac{V_p(1)}{I_{\sqrt{\omega_2}}(\sqrt{\omega_1})} I_{\sqrt{\omega_2}}(\sqrt{\omega_1}r), \tag{32}$$

where $V_p(r) = \sum_{n=0}^{\infty} a_n r^n$,

$$\text{with} \quad a_n = \begin{cases} 0 & \text{for } n = 0 \text{ or } n \text{ odd} \\ \dfrac{\omega_3}{4 - \omega_2} & \text{for } n = 2 \\ \dfrac{\omega_1 a_{n-2}}{n^2 - \omega_2} & \text{for } n \text{ even, } n > 2 \end{cases} \tag{33}$$

$$\text{and} \quad \omega_1 = \frac{r_\xi + \frac{4}{3}}{R^2(B - \frac{D^2}{A-C+1})}, \quad \omega_2 = \frac{C + 2}{B - \frac{D^2}{A-C+1}}, \quad \omega_3 = \frac{D}{(A - C + 1)B - D^2}. \tag{34}$$

Here I_ν denotes the modified Bessel function of the first kind of order ν. This is the solution for any constant α and Θ, provided $\omega_2 \neq n^2$ for $n = 0, 2, 4, 6, 8, \ldots$.

Having found the radial velocity, the vertical velocity which satisfies $V_z^0(1) = 0$ is given by

$$V_z^0 = \frac{r^2 - 1}{4(A - C + 1)} + \frac{D}{A - C + 1} V_r^0. \tag{35}$$

We can now also get a solution for $P_0(r)$ from equation (20).

Alternatively, the system of linear ODEs for V_r^0, V_z^0 and P_0 can be solved numerically. See figure 1 for results of numerical integration using the *Chebfun* software. For information on *Chebfun* and chebops, see Trefethen and Driscoll [2011], Trefethen [2013], Driscoll et al. [2008].

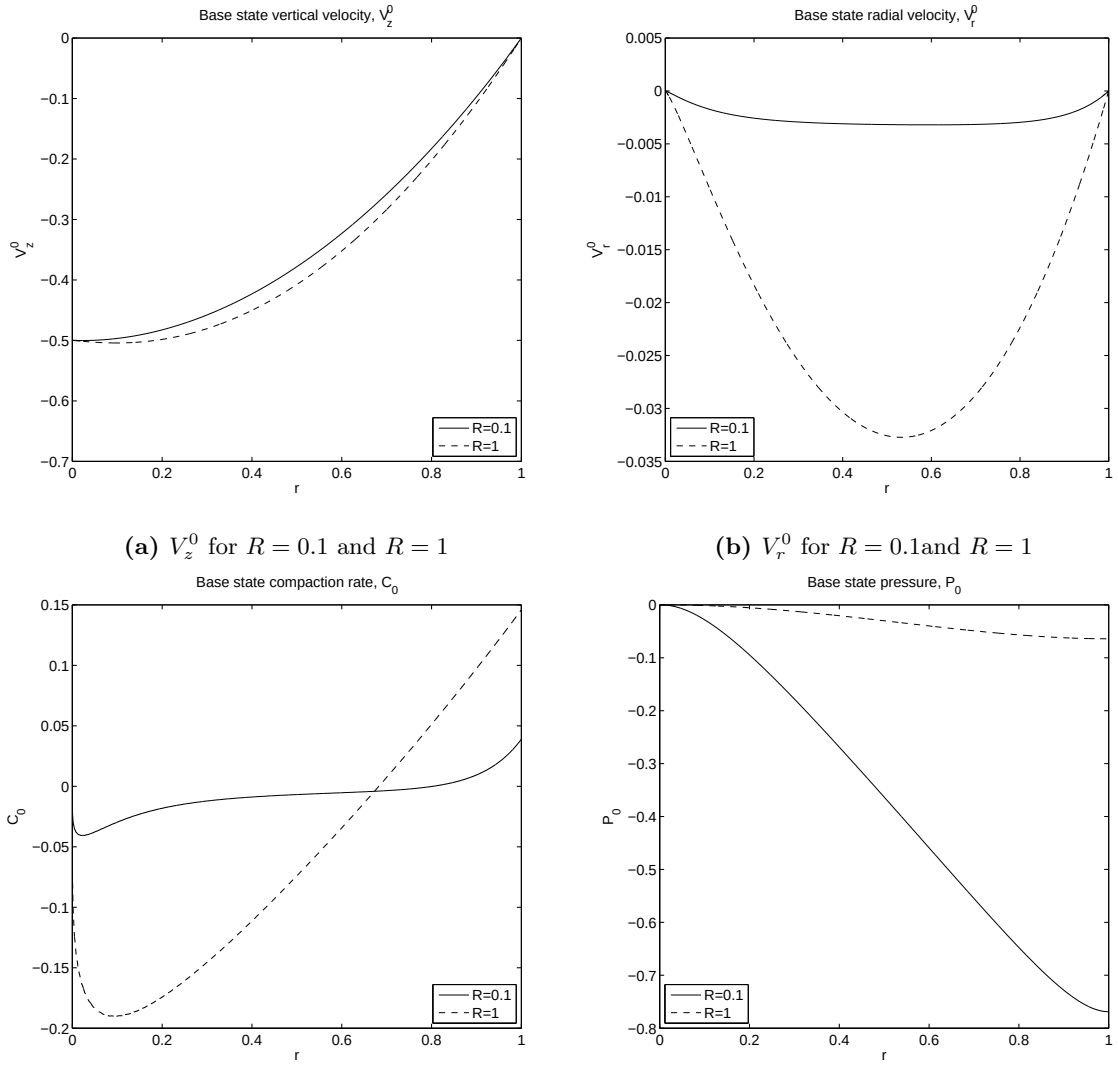

(a) V_z^0 for $R = 0.1$ and $R = 1$

(b) V_r^0 for $R = 0.1$and $R = 1$

(c) C_0 for $R = 0.1$and $R = 1$

(d) P_0 for $R = 0.1$and $R = 1$

Figure 1: Solution at $\tau = 0$, with $\alpha = 2$, $\Theta = \frac{\pi}{4}$, $r_\xi = \frac{5}{3}$. Solid lines indicate $R = 0.1$ and dashed lines indicate $R = 1$.

Using the series representation of the modified Bessel function [Baricz, 2010], we see that the condition $\dfrac{\partial V_z^0}{\partial r} = 0$ at $r = 0$ will be satisfied if and only if $\omega_2 > 1$, as this is when $I_{\sqrt{\omega_2}}$ has zero derivative at the origin. Either way, the solution is not analytic at $r = 0$ (unless $\sqrt{\omega_2}$ happens to be an integer). This problem is a result of the assumption that $\Theta \neq 0$ in the centre. If we were to use a model in which $\Theta = 0$ at $r = 0$, then $V_r^0 = 0$ and $\dfrac{\partial V_z^0}{\partial r} = 0$ at $r = 0$ would follow straight away from equations (30) and (31).

At $\tau = 0$, $\dfrac{\partial \phi}{\partial \tau} = (1 - \phi_0)\mathcal{C}_0$, so the plots of $\mathcal{C}_0$ in figure 1 predict that the porosity will increase at larger radii and decrease at smaller radii, i.e. the liquid will move outwards towards the boundary. However, figure 1 indicates a problem with the solution at $r = 0$. We really require that $\dfrac{\partial \mathcal{C}_0}{\partial r} = 0$ at $r = 0$, since $\mathcal{C}_0$ should be an

even function of r. When we make use of equation (31) we find that

$$\frac{\partial \mathcal{C}_0}{\partial r} = \omega_3 + \omega_1 V_r^0 + \frac{(\omega_2 - 1)V_r^0}{r^2}, \tag{36}$$

which will indeed be 0 at $r = 0$ under a model of Θ satisfying the symmetry condition that $\Theta = 0$ at $r = 0$, but is infinite under the current constant anisotropy assumption.

The problem of $\mathcal{C}_0$ having infinite derivative at the centre is also evident in both the planar Poiseuille and the torsion analysis of Katz and Takei [2013a], resulting from (respectively) the assumptions of non-zero Θ and non-zero α at the origin. For torsion, as for pipe Poiseuille, the radial velocity equation under the uniform anisotropy assumption (see Katz and Takei [2013a]) predicts a non-analytic V_r^0. The velocity in the plane Poiseuille case, given in section 3.4.1, becomes problematic when the solution is continued to the whole of $-1 \leq x \leq 1$ with the appropriate symmetry.

3.3 Growth of porosity perturbations at $\tau = 0$

Before considering the problem of finding a model of Θ and α that is physically possible, I consider the growth of harmonic perturbations to the base flow. The following calculations for the leading order growth rate will be valid whether A, B, C, D, E, F are constants or non-constants.

The $O(1)$ terms in the equations already balance; now we concentrate on balancing those of order ε. We have three equations — coming from (19), (20) and (21) — which determine P_1, V_r^1 and V_z^1; we then find the value of $\dfrac{\partial \phi_1}{\partial \tau}$ at $\tau = 0$ from equation (18).

We consider perturbations of the form

$$\phi_1(r, z, \tau) = exp\left(i\mathbf{k} \cdot \left(\mathbf{x} - \int_0^\tau \mathbf{V^0} \mathrm{d}t\right) + \psi(r, z, \tau)\right) \tag{37}$$

where $\mathbf{k} = k_r \hat{\mathbf{r}} + k_z \hat{\mathbf{z}}$ with k_r and k_z constants, and we define

$$k = \sqrt{k_r^2 + k_z^2}, \tag{38}$$

$$s + i\Omega = \frac{\partial \psi}{\partial \tau}, \tag{39}$$

$$\text{with} \quad \nabla\psi,\ \nabla(s + i\Omega) = o(k) \text{ as } k \to \infty. \tag{40}$$

At $\tau = 0$ these are cones of locally harmonic waves moving with the base state flow, and equation (40) is interpreted as saying that both ψ and the growth rate $s + i\Omega$ are 'slowly varying' in space (they only vary over a lengthscale much longer than the wavelength). Fixing $\tau = 0$, neglecting all but the leading order terms as $k \to \infty$, and writing

$$V_r^1 = \tilde{V}_r \phi_1, \quad V_z^1 = \tilde{V}_z \phi_1, \quad P_1 = \tilde{P} \phi_1, \tag{41}$$

with $\tilde{V}_r$, $\tilde{V}_z$ and $\tilde{P}$ also only slowly varying, the equations can be inverted to give expressions for $\tilde{P}$, $\tilde{V}_r$ and $\tilde{V}_z$ which are valid to leading order. Then to obtain the growth rate, we use equation (18), leading to

$$s + i\Omega \sim (1 - \phi_0)(ik_r \tilde{V}_r + ik_z \tilde{V}_z) - \nabla \cdot \mathbf{V^0} \tag{42}$$

as $k \to \infty$, to find that the growth rate at $\tau = 0$, to leading order in k, is

$$s \sim \frac{1 - \phi_0}{N_3 N_6 - N_4 N_5}[(N_1 N_6 - N_2 N_5)W_1 + (-N_1 N_4 + N_2 N_3)W_2] - \mathcal{C}_0 \tag{43}$$

where

$$N_1 = ik_r, \tag{44}$$

$$N_2 = ik_z, \tag{45}$$

$$N_3 = Bk_r^2 + (A - C + 1)k_z^2 - 2Dk_r k_z, \tag{46}$$

$$N_4 = -Dk_r^2 - Ek_z^2 + (2A - C + 1)k_r k_z, \tag{47}$$

$$N_5 = -Dk_r^2 - Ek_z^2 + (2A - C + 1)k_r k_z, \tag{48}$$

$$N_6 = (A - C + 1)k_r^2 + Fk_z^2 - 2Ek_r k_z, \tag{49}$$

and

$$W_1 = -\lambda i k_r (B\frac{\partial V_r^0}{\partial r} + C\frac{V_r^0}{r} - D\frac{\partial V_z^0}{\partial r}) - \lambda i k_z (-D\frac{\partial V_r^0}{\partial r} + (A - C + 1)\frac{\partial V_z^0}{\partial r}), \tag{50}$$

$$W_2 = -\lambda i k_r (-D\frac{\partial V_r^0}{\partial r} + (A - C + 1)\frac{\partial V_z^0}{\partial r}) - \lambda i k_z (A\frac{\partial V_r^0}{\partial r} + C\frac{V_r^0}{r} - E\frac{\partial V_z^0}{\partial r}). \tag{51}$$

We also find that $\Omega = o(1)$ as $k \to \infty$, and that (since $s = O(1)$) we have found all the terms of $s + i\Omega$ which do not decay in this limit.

In the isotropic case, $\alpha = 0$, the above result for the growth rate s reduces to

$$s \sim \frac{(1 - \phi_0)\lambda r k_r k_z}{(r_\xi + \frac{4}{3})k^2} \tag{52}$$

as $k \to \infty$. Let us write

$$\mathbf{k} = k(\cos\theta \hat{\mathbf{r}} + \sin\theta \hat{\mathbf{z}}); \tag{53}$$

then as $k \to \infty$ the growth rate s is proportional to $\sin(2\theta)$ and so is largest for the perturbations with angle $\theta = 45°$. This is illustrated in figure 2a.

With constant, non-zero, values of Θ and α, 45° is no longer the most favourable angle for growth. Figures 2b and 2c show how the leading order growth rate s varies with the angle θ of the perturbation when $\Theta = \frac{\pi}{4}$ and $\alpha = 2$. These show that one effect of the anisotropy is to split the peak seen in figure 2a into two peaks (corresponding to the fastest growing disturbances at $\tau = 0$), one at an angle less than 45° and one at an angle greater than 45°. This effect was also found by Katz and Takei [2013a] who applied this theoretical approach to simple shear, plane Poiseuille and torsion. The positions and relative heights of the peaks depend on the value of the anisotropy angle Θ. In the case $\Theta = \frac{\pi}{4}$ (figures 2b and 2c), the peaks occur at angles of approximately 14–15° and 72–74°. For values of constant Θ less than $\frac{\pi}{4}$, the low-angle peak is dominant, and occurs at an angle larger than 15°.

3.4 Comparison with constant anisotropy plane Poiseuille flow at $\tau = 0$

3.4.1 Base state

We compare pipe and plane Poiseuille results for constant α, and $\Theta = \frac{\pi}{4}$, when the velocity has been non-dimensionalised using the scaling $U = \dfrac{\rho g H^2}{\eta_0}$, where H is either the radius of the cylinder or half the width of the channel.

The planar solution in this case (in the x-z plane) has the following base state velocity on $0 \le x \le 1$:

$$V_x^0 = \frac{R^2\alpha}{(r_\xi + \frac{4}{3})(4 - \alpha)} \left(\frac{\sinh\frac{\beta x}{R}}{\sinh\frac{\beta}{R}} + \frac{\sinh\frac{\beta(1-x)}{R}}{\sinh\frac{\beta}{R}} - 1 \right), \tag{54}$$

$$V_z^0 = \frac{2}{4 - \alpha}(x^2 - 1) + \frac{\alpha}{4 - \alpha} \left(V_x^0 - (x - 1)\left.\frac{\partial V_x^0}{\partial x}\right|_{x=0} \right), \tag{55}$$

where $\beta = \sqrt{\dfrac{r_\xi + \frac{4}{3}}{r_\xi + \frac{4}{3} - \frac{\alpha}{4-\alpha}}}$. This solution is computed by solving the equations in Cartesian coordinates on $0 \le x \le 1$ and applying boundary conditions $V_x^0 = \dfrac{\partial P_0}{\partial x} = \dfrac{\partial V_z^0}{\partial x} = 0$ at $x = 0$, and $V_x^0 = V_z^0 = 0$ at $x = 1$.

The solutions for the base state velocities in two geometries are very similar but there are notable differences. Figure 3 compares $\mathbf{V^0}$ for plane and pipe Poiseuille when $R = 0.1$, and with $\alpha = 2$, $\Theta = \frac{\pi}{4}$, and $r_\xi = \frac{5}{3}$. It shows that the horizontal velocities are approximately equal in both shape and magnitude. (In fact there are differences at $r = 0$, with the radial pipe flow having zero derivative there.) The two vertical velocities have almost the same shape, but differ by a factor of two (as we expect when we consider the solutions to isotropic Poiseuille flow in the two different geometries). So one difference in the cylindrical geometry appears to be that there is a larger ratio of the horizontal to vertical velocity components than there is in in the planar case.

3.4.2 Growth of porosity perturbations

The plots of the growth rates are remarkably similar to the corresponding plots for plane Poiseuille [Katz and Takei, 2013a]. Indeed, when we compare the equations in the pipe and plane geometries, and consider any term in which $\frac{\partial}{\partial r} + \frac{1}{r}$, instead of just $\frac{\partial}{\partial x}$ in the planar case, is applied to the perturbation variables (with index 1), we see that the extra term (coming from the curved geometry) is neglected, since it is of a lower order in k than the term coming from the derivative. Nevertheless, there are 'cylindrical' terms (e.g. $\frac{V_r^0}{r}$) which appear in W_1 and W_2, showing that the growth rates still depend in some way on the cylindrical geometry.

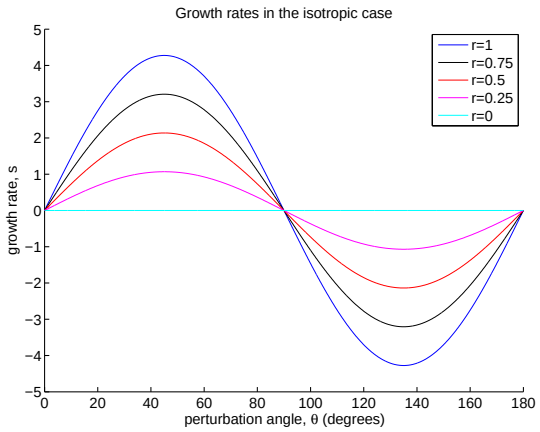

(a) Predicted growth rate for $R = 1$ in the isotropic case $\alpha = 0$.

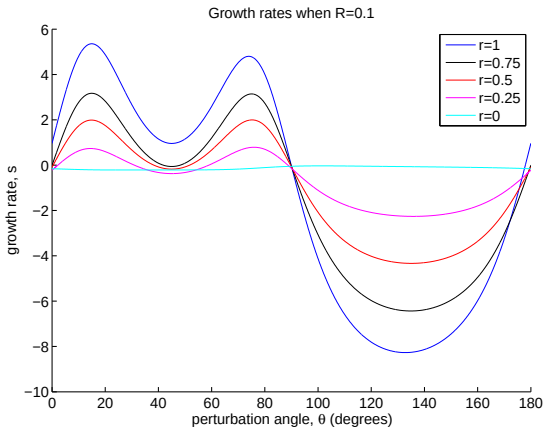

(b) Predicted growth rate for $R = 0.1$, with $\alpha = 2$ and $\Theta = \frac{\pi}{4}$.

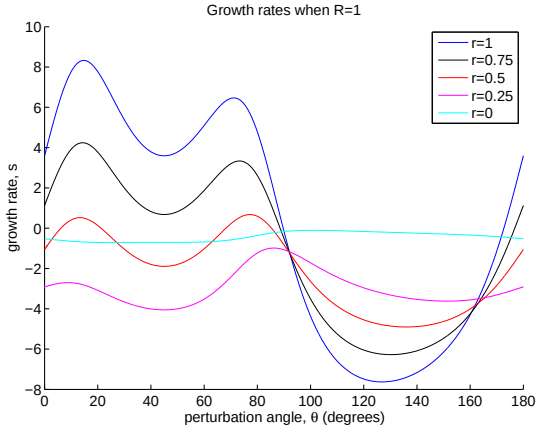

(c) Predicted growth rate for $R = 1$, with $\alpha = 2$ and $\Theta = \frac{\pi}{4}$.

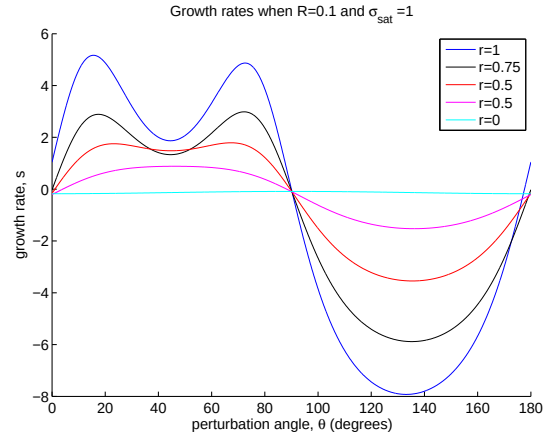

(d) Predicted growth rates using the new model for Θ and α, and $R = 0.1$, $\sigma_{sat} = 1$.

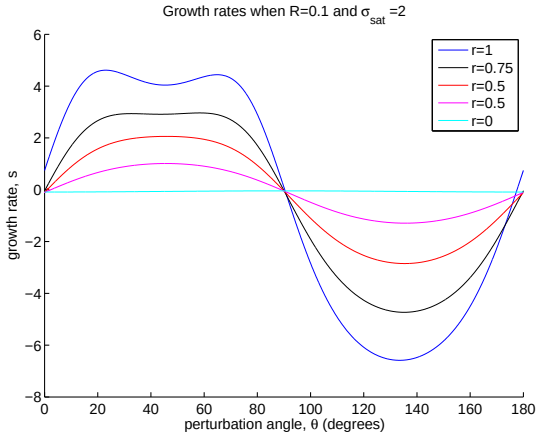

(e) Predicted growth rates using the new model for Θ and α, and $R = 0.1$, $\sigma_{sat} = 2$.

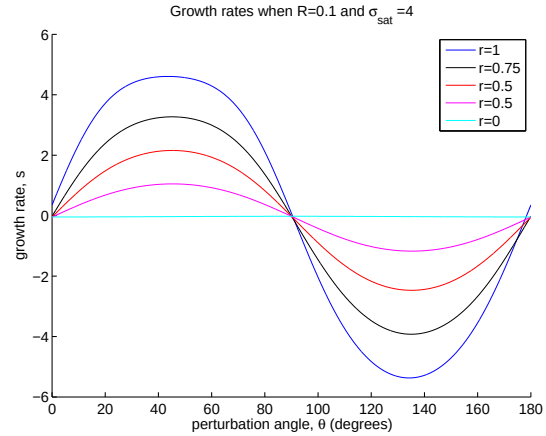

(f) Predicted growth rates using the new model for Θ and α, and $R = 0.1$, $\sigma_{sat} = 4$.

Figure 2: Predicted growth rates, s, as a function of perturbation angle θ: in the isotropic case (2a); with the uniform anisotropy model (2b, 2c); and with the new approximate forms of Θ and α in equations (60)–(62) (2d, 2e, 2f). Here $r_\xi = \frac{5}{3}$, $\lambda = 27$, $\phi_0 = 0.05$ and $n = 2$.

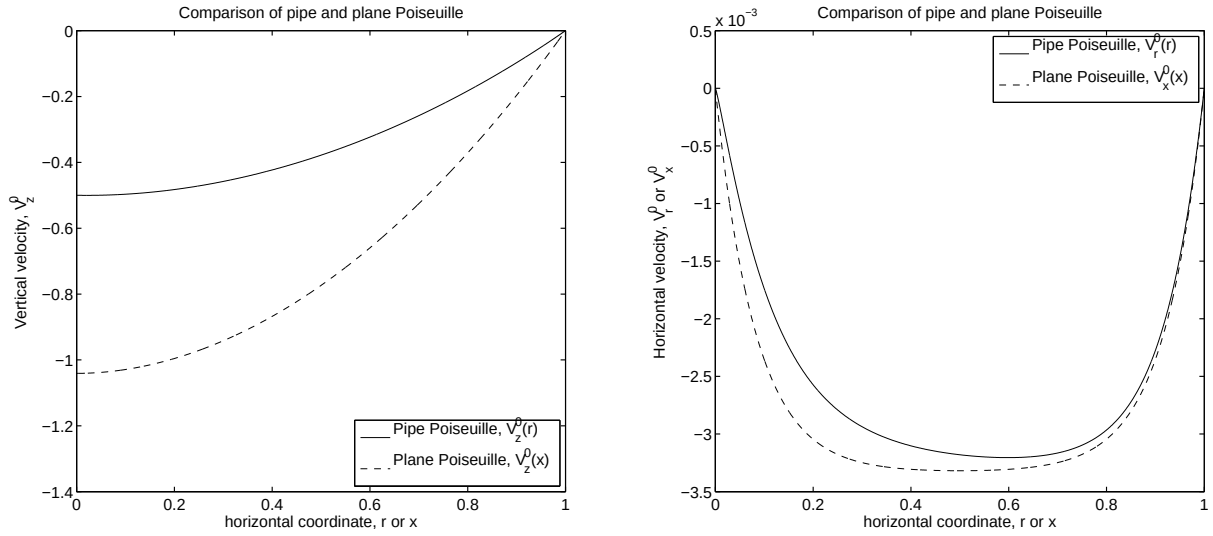

(a) Vertical velocities for pipe and plane Poiseuille flow. **(b)** Horizontal velocities for pipe and plane Poiseuille flow.

Figure 3: Comparison of pipe Poiseuille (solid line) and plane Poiseuille (dashed line) base state velocities when $R = 0.1$, $\alpha = 2$, $\Theta = \frac{\pi}{4}$, $r_\xi = \frac{5}{3}$.

4 Variable anisotropy analysis

4.1 Non-uniform model for initial anisotropy

So far, we have considered the angle of anisotropy (measured from the vertical) to be constant. As we have already noted, this is not possible for physical reasons, creating problems at $r = 0$. If the equations do not represent a physically possible situation at the centre then nor will the solution.

Another important consideration is how well the model used for Θ represents what it is intended to, namely the angle between the z-axis and the maximum principal stress. There is also a theory for how α should depend on the components of the stress tensor, and we would like a model which agrees with it. According to the model presented in Katz and Takei [2013a], the expressions from which we determine Θ and α are:

$$\cos(2\Theta) = \frac{\sigma_{zz} - \sigma_{rr}}{\sigma_3 - \sigma_1}, \quad \sin(2\Theta) = \frac{2\sigma_{rz}}{\sigma_3 - \sigma_1}, \tag{56}$$

$$\alpha = 2\tanh\left(\frac{2(\sigma_3 - \sigma_1)}{\sigma_{sat}}\right), \tag{57}$$

where σ_{sat} is a constant depending on the material. These equations give

$$2\Theta = \arg(2\sigma_{rz}i + \sigma_{zz} - \sigma_{rr}), \tag{58}$$

$$\alpha = 2\tanh\left(\frac{4\sigma_{rz}}{\sigma_{sat}\sin(2\Theta)}\right) = 2\tanh\left(\frac{2(\sigma_{zz} - \sigma_{rr})}{\sigma_{sat}\cos(2\Theta)}\right). \tag{59}$$

(Both here and below, "arg" is the complex argument of the number in the range $(-\pi, \pi]$, and will be found using the *MatLab* function *atan2*.)

Figures 4a and 4b illustrate that for small values of the non-dimensionalised compaction length R, the assumption $\Theta = \frac{\pi}{4}$ gives a self-consistent result on much of the domain, but fails in a region near $r = 0$. For $R = 1$ the assumption that $\Theta = \frac{\pi}{4}$ is even more strongly contradicted by the solution, with Θ varying gradually across the whole domain. Similarly, the assumption of constant α will not be consistent with the solution.

There is a need, not only for a model which obeys the conditions for Θ and α at $r = 0$, but for one which is consistent. Here, we have considered alternative forms of Θ and α to put into the equations before solving them, with the aim to find a more consistent model and solution for the base state. This method (specifying forms of Θ and α before solving the differential equations) will retain the advantage that the differential equations are linear in V_r^0 and V_z^0. As such, we are able to continue using linear chebops and the *Chebfun* software to integrate the differential equations. (In contrast, the full equations are non-linear.) It may also be advantageous to have analytic expressions giving the approximate forms of the anisotropy parameters Θ and α.

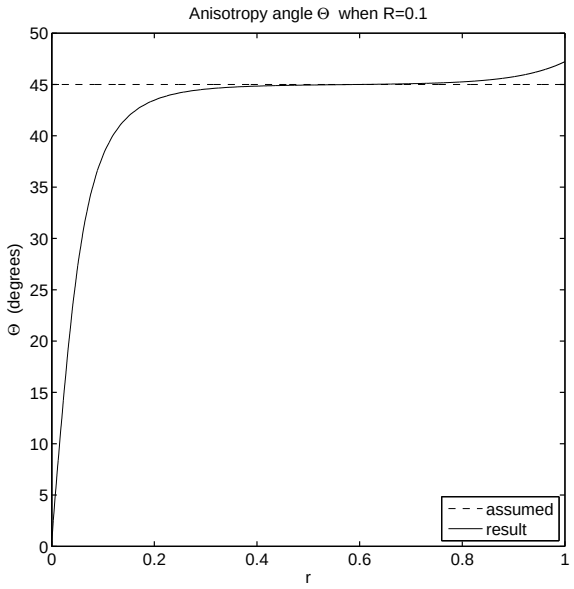

(a) Plot of Θ (in degrees) vs r for $R = 0.1$, showing validity of the assumption except near $r = 0$.

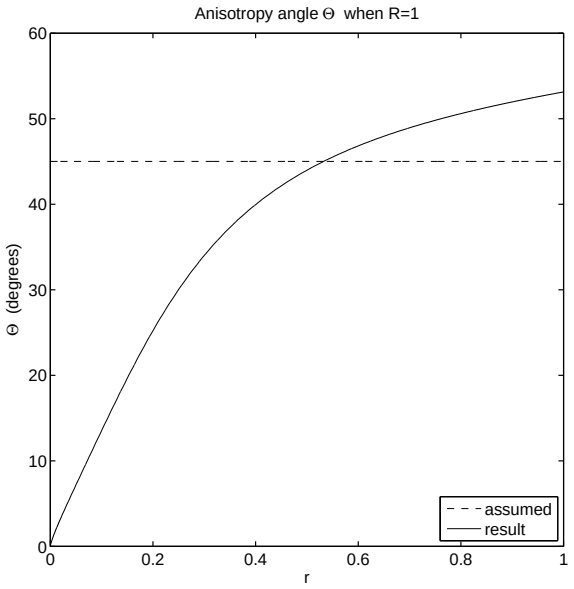

(b) Plot of Θ (in degrees) vs r for $R = 1$, showing invalidity of the assumption used.

Figure 4: Plots of Θ (in degrees) vs r investigating whether the assumption was valid.

With a model of the form

$$\Theta = \frac{1}{2}\arg(ri + f_1(r)), \quad \alpha = 2\tanh\left(f_2(r)\right), \tag{60}$$

$$\text{with} \quad f_1(r) = m_1(1-2r), \quad \text{and} \quad f_2(r) = \frac{2r}{\sigma_{sat}} + m_2 \exp\left(-\frac{2r}{m_2\sigma_{sat}}\right) \tag{61}$$

(where m_1 and m_2 are constants which may depend on R and σ_{sat}), a reasonable level of self-consistency can be achieved. For large ranges of R and σ_{sat}, suitable expressions for the constants m_1 and m_2 are

$$m_1 = \tanh R \times \left(0.3\exp\left(-0.6\sigma_{sat}\right) + 0.03\right), \quad m_2 = \frac{2m_1}{\sigma_{sat}}. \tag{62}$$

Note that, unlike before, these expressions for the anisotropy parameters satisfy $\Theta = 0$ and $\dfrac{\partial\alpha}{\partial r} = 0$ at $r = 0$, and so we expect the corresponding solution to be more regular at the centre. However for a model which is completely smooth at $r = 0$ (and hence a completely smooth solution), we really require f_1 and f_2 to be even functions of r.

The self-consistency of the model defined by equations (60)–(62) is illustrated by examples in figure 5. These graphs (together with similar results for other values of R and σ_{sat}) confirm that a model of this form is more consistent. A further check that this model is an improvement is given in figure 6, which shows that $\mathcal{C}_0$ now has zero derivative at $r = 0$. Having achieved both regularity at the level we are considering, and consistency, we conclude that (provided we do not want to take any more derivatives) the chosen forms of f_1, f_2, m_1 and m_2 are reasonable approximations, and we leave the possible development of a smooth model for future work.

Figure 6 also shows that at larger radii, the two models give similar compaction/decompaction rates, and that the prediction of increasing porosity at the boundary was correct.

Figure 7 compares the solutions computed with the original (uniform α and Θ) model and the new model proposed above. The numerical solution of the full non-linear equations — which will be discussed in section 4.2 — is also plotted, indicating that (unless we start taking more derivatives) the new model of Θ and α gives a very good approximation to the true solution at $\tau = 0$.

With the new model, we can also consider the growth rate s of perturbations. The leading order growth rate of the perturbations considered in section 3.3 are still given by equation (43), but now the quantities A to F are non-constant. Results are plotted in figures 2d, 2e and 2f. When $\sigma_{sat} \leq 1$ (figure 2d) the plots of s are very similar to before, and the peaks occur for approximately the same angles θ as were found earlier, at $\approx 15°$ and $\approx 72.5°$. But for larger σ_{sat}, the plots of s become more similar to the isotropic case, without the low- and high-angle peaks, but with just one peak at $\theta = 45°$. (See figure 2f.) For intermediate values of σ_{sat} (figure 2e), perturbations of all angles between about 20° and 80° are predicted almost equal growth rates.

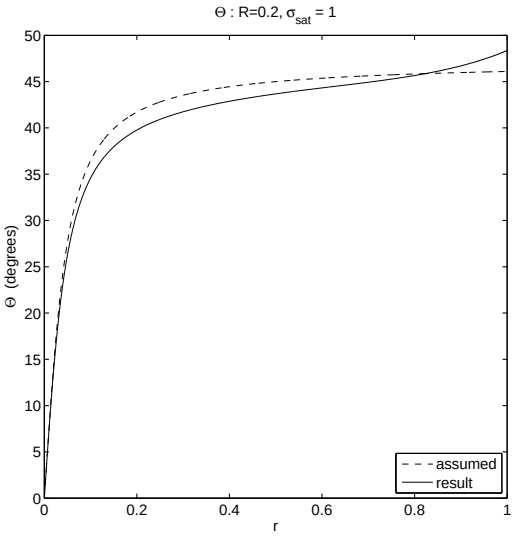

(a) Assumed and resulting forms of Θ (in degrees). Here $R = 0.2$, $\sigma_{sat} = 1$ and $r_\xi = \frac{5}{3}$.

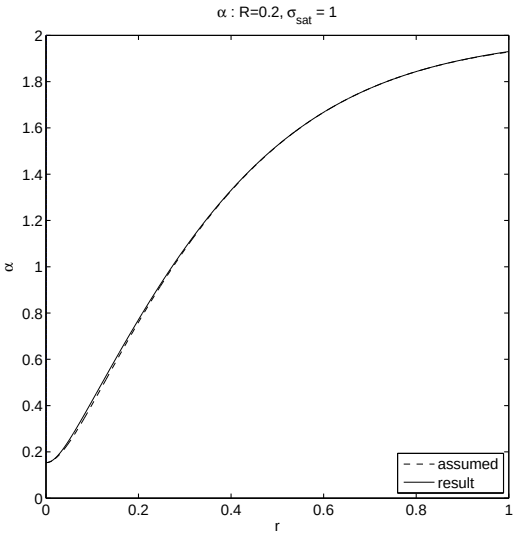

(b) Assumed and resulting forms of α. Here $R = 0.2$, $\sigma_{sat} = 1$ and $r_\xi = \frac{5}{3}$.

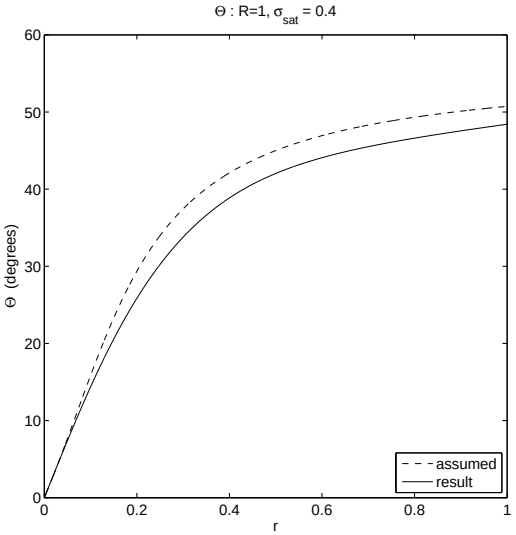

(c) Assumed and resulting forms of Θ (in degrees). Here $R = 1$, $\sigma_{sat} = 0.4$ and $r_\xi = \frac{5}{3}$.

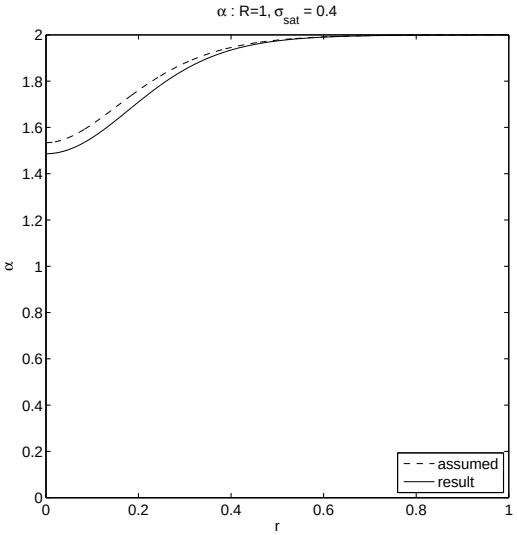

(d) Assumed and resulting forms of α. Here $R = 1$, $\sigma_{sat} = 0.4$ and $r_\xi = \frac{5}{3}$.

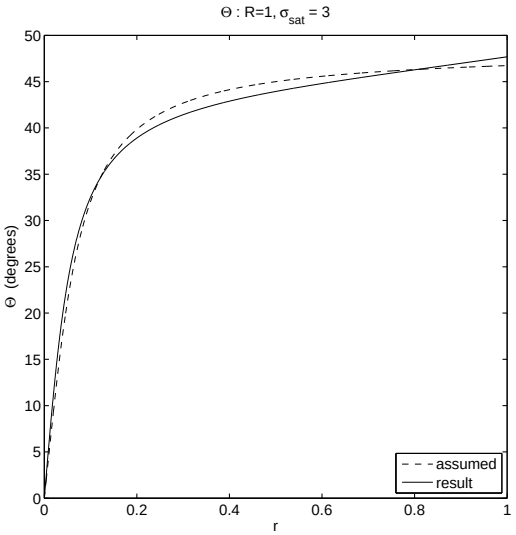

(e) Assumed and resulting forms of Θ (in degrees). Here $R = 1$, $\sigma_{sat} = 3$ and $r_\xi = \frac{5}{3}$.

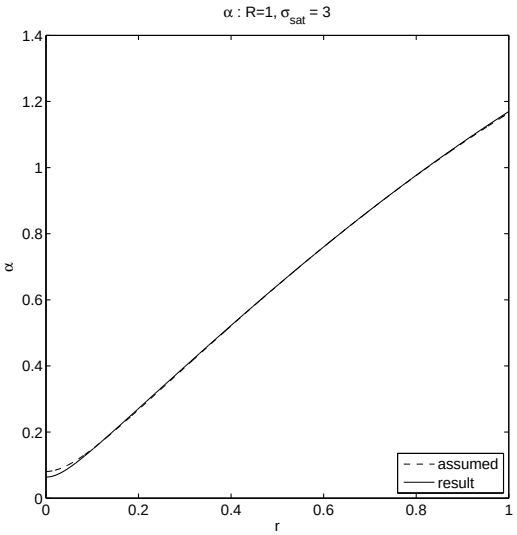

(f) Assumed and resulting forms of α. Here $R = 1$, $\sigma_{sat} = 3$ and $r_\xi = \frac{5}{3}$.

Figure 5: Assumed and resulting forms of Θ and α in the new model. Some examples.

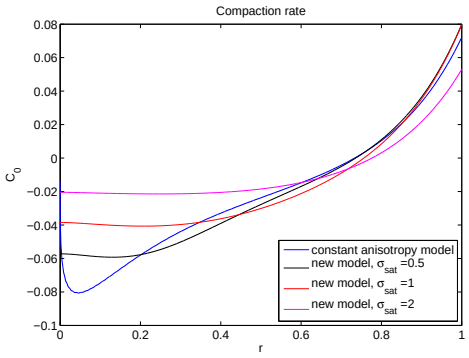

Figure 6: Compaction rate at $\tau = 0$, comparing the solutions obtained with the new and original models for Θ and α. Here $R = 0.2$ and $r_\xi = \frac{5}{3}$.

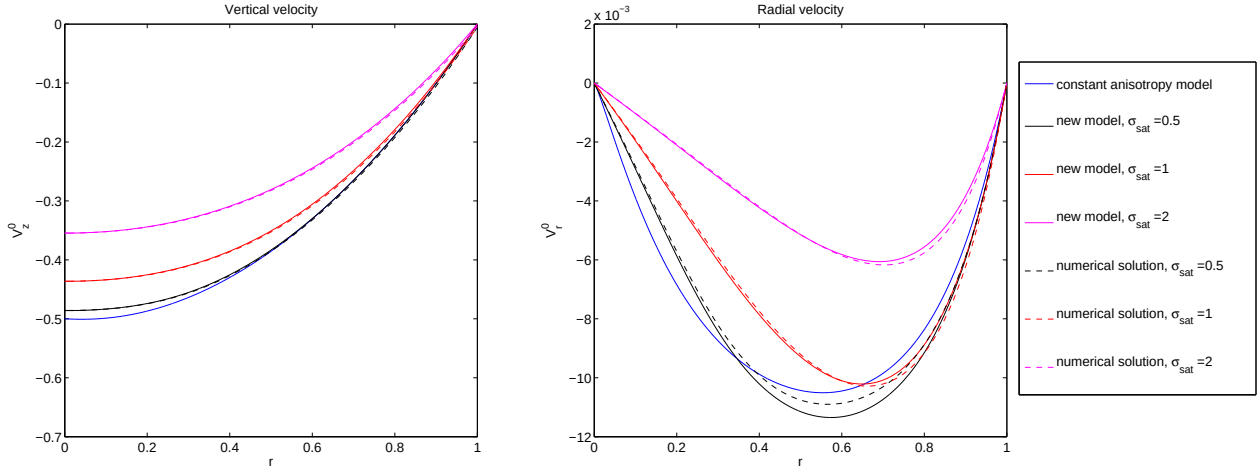

Figure 7: Base state velocity at $\tau = 0$, comparing the solutions obtained with the new and original models for Θ and α, and the numerical solution (dashed lines). Here $R = 0.2$ and $r_\xi = \frac{5}{3}$.

4.2 Numerical solution of the full equations

In this section, the governing non-linear differential equations are solved numerically. At a fixed time, using the viscosity tensor and the porosity from the previous time step, the partial differential equations (19), (20) and (21) are discretised in space using finite difference approximations to derivatives. This yields a system of non-linear algebraic equations, which are solved for the velocity and pressure using Newton's method. Then, using a finite difference approximation to equation (18) to implement a forward time-step, the porosity is updated. This is the method described in Katz and Takei [2013b], and is implemented using the Portable, Extensible Toolkit for Scientific Computation (PETSc), discussed in more detail by Katz et al. [2007].

The values of parameters used are $n = 2$, $r_\xi = \frac{5}{3}$, $\lambda = 27$, and $\phi_0 = 0.05$, and the numerical solution for $\tau \geq 0$ is investigated. Since the model is based on the assumption that ϕ is small, we consider only the results at small times τ, when the porosity remains less than 0.1 throughout the domain.

4.2.1 Base state

The program is set to add "white noise" to the initial porosity, of a specified maximum amplitude. For the base state, for which we require an initially uniform porosity, the amplitude of the white noise is set to 10^{-9}.

From the solution at $\tau = 0$, we know that the porosity is increasing at larger radii and is decreasing nearer the centre. Figure 8a shows the porosity field solution at times $\tau = 0.00, 0.04, 0.08, 0.12, 0.16, 0.20$, while figures 8b and 8c plot the radial and vertical velocity components at these times. It is worth noting briefly that the anisotropy parameters Θ and α do evolve in time, but do not experience large changes over the time interval considered here.

As time passes, the model predicts that the peak radial velocity moves outwards and that more and more liquid moves to the boundary. The solution also predicts a downward acceleration which is increasing in time.

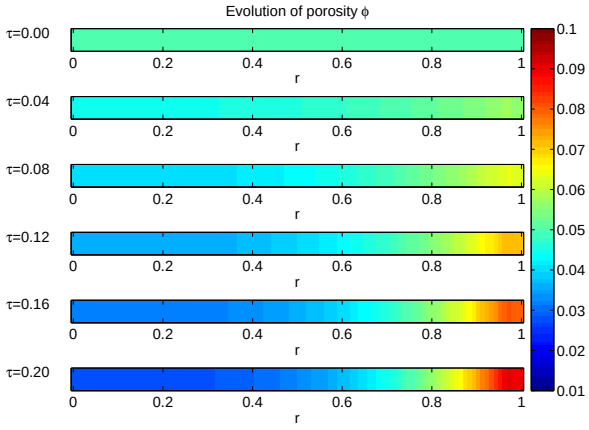

(a) Porosity between $\tau = 0$ and 0.20.

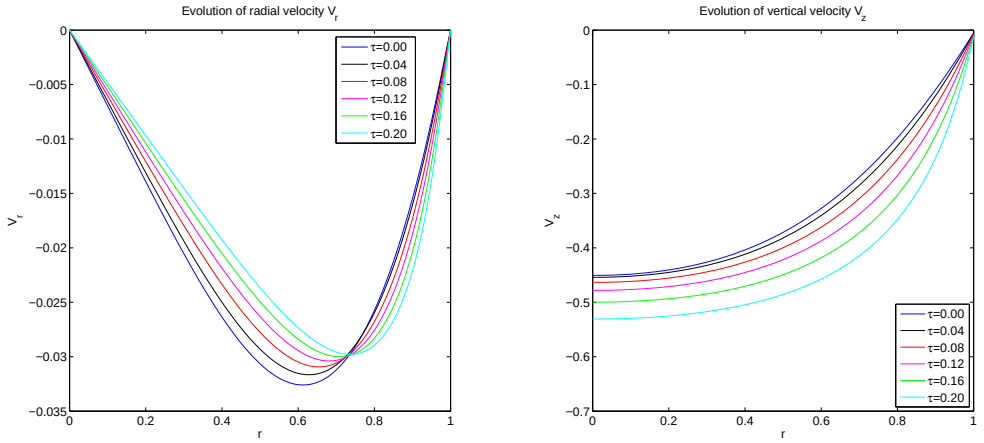

(b) Radial velocity between $\tau = 0$ and 0.20.

(c) Vertical velocity between $\tau = 0$ and 0.20.

Figure 8: Base state evolution of the porosity and velocity fields between $\tau = 0$ and $\tau = 0.20$. Here $R = 1$, $\sigma_{sat} = 1$, $n = 2$ and $r_\xi = \frac{5}{3}$. Similar results (sometimes over a different time scale) are obtained with other parameter values.

4.2.2 Growth of porosity perturbations

To investigate the development of small perturbations, white noise is added to the (otherwise uniform) initial porosity. Figure 9 shows the porosity field in three cases (corresponding to $R = 0.05$, $R = 0.1$ and $R = 0.3$), having evolved from an initial porosity of $\phi_0 = 0.05$ with white noise added to a maximum amplitude of 0.01. Similar results are generated when $n = 3$ and when σ_{sat} takes different values.

The results show a similar outcome to the unperturbed system, with the fluid moving towards the walls of the pipe. At the very edge of the pipe, the fluid begins to accumulate in a thin layer.

However, this is no longer the only development of the porosity field. Now, as an effect of the perturbation, there is some evidence of porosity bands forming. These form quite near the edges, but before the region of very high porosity. Our results show the bands forming at angles of $\approx 20°$ to the vertical. These bands only represent a small difference in porosity (especially when compared to the build-up at the wall of the cylinder), but they occur consistently, and at the same angle, in simulations with small values of R. As R becomes larger ($R \geq 0.2$, say), the bands are no longer visible. This is illustrated in the final plot of figure 9.

For comparison, figure 10 shows the results of running the numerical simulation with α and Θ set to 0 (i.e. the isotropic case), and an initial random porosity perturbation. These plots show that porosity bands are also predicted in the isotropic case, but that their angle to the vertical is close to 45°. In the isotropic case the bands are predicited not just for small R but also for $R = 1$.

5 Discussion

Here we have investigated the effects on anisotropic viscosity on pipe Poiseulle flow (using a particular model of the viscosity tensor).

While it is extremely useful to compare these predictions with experiments, there are several differences between the system considered in this work and the experimental procedure. In experiments, material is often

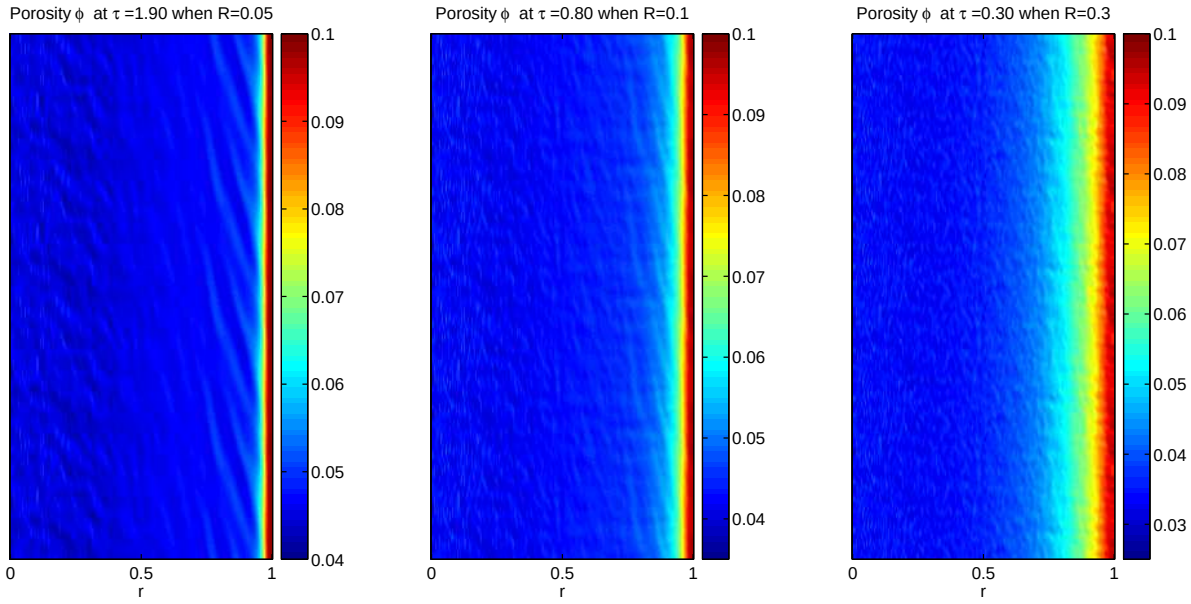

(a) Porosity after evolving for a time $\tau = 1.90$, when $R = 0.05$.

(b) Porosity after evolving for a time $\tau = 0.80$, when $R = 0.1$.

(c) Porosity after evolving for a time $\tau = 0.30$, when $R = 0.3$.

Figure 9: Porosity fields showing the migration of magma to the edge of the domain and, for small R, high-porsity bands at approximately 20° to the vertical. Here the parameters take values $\sigma_{sat} = 1$, $n = 2$, $\phi_0 = 0.05$, and a random perturbation of maximum amplitude 0.01 was added to the initial porosity. The grid uses 204 gridpoints by 400, and the times were chosen so that the maximum porosity is just less than 0.10.

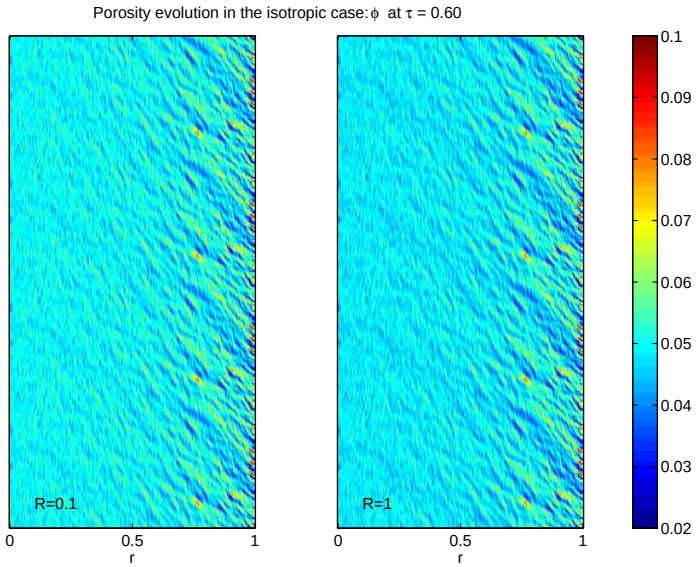

Figure 10: In an isotropic system high-porosity bands form at approximately 45° to the vertical. Here the parameters take values $n = 2$, $\phi_0 = 0.05$, and a random perturbation of maximum amplitude 0.01 was added to the initial porosity. The grid uses 204 gridpoints by 400, and the times were chosen so that the maximum porosity is just less than 0.10.

forced through the pipe under high pressure, whereas here we consider the driving force to be gravitational. Here, too, we consider an infinitely long pipe which is clearly not achievable in practice. Instead, a finite tube is used and fluid is inserted at one end. The boundary conditions will therefore be very different in the experimental configuration — but it will still be interesting to compare the observed flow in the central region of the pipe with the above results. One other important difference is that we have considered only axisymmetric flow and axisymmetric perturbations. In practice any disturbances to the initial porosity are unlikely to be axisymmetric, and we have not here considered how such perturbations would be expected to grow. This is a possible basis for further investigation.

First we considered a base state with an initially uniform porosity, and used the equations to predict matrix compaction driving the fluid radially outwards. This base state segregation is in contrast to what is found for an isotropic system, which has zero radial velocity and in which the porosity field does not evolve in time.

Then we considered theoretical growth rates of disturbances to the porosity field at $\tau = 0$. The perturbations whose growth rates were considered were just one very particular type of perturbation. It is unclear how much can be determined about general disturbances by considering these axisymmetric, locally harmonic waves at $\tau = 0$, with asymptotically short wavelength. But what the theoretical work does show is that the development of perturbations is expected to be quite different from development of perturbations in an isotropic medium. The results also start to suggest why high porosity bands may form at angles of $\approx 15^\circ$ to the vertical, whereas angles of 45° (favoured in the isotropic system) are less favourable for growth.

In the numerical simulation we added random noise to the initial porosity, and found that over time, high-porosity bands formed at an angle to the vertical which was similar (but not identical) to an angle having a high theoretical growth rate. The numerical solutions at later times also continue to predict liquid migration to the boundary.

The effects of an anisotropic viscosity for pipe Poiseuille flow are similar to those predicted by Katz and Takei [2013a,b] for plane Poiseuille flow, both in terms of the base state segregation of the liquid towards the wall and in terms of the development of high-porosity bands at an angle of about 15–20° to the vertical.

When the anisotropic viscosity results are compared with experimental results we see some similarities (in general terms), but also some major differences as time passes. The experiments do produce bands at low angles ($\approx$ 15–20°) to the vertical. It is worth investigating whether these bands form at all values of R or just at small R, as our results only showed visible bands when R was less than about 0.2. Experimental observations also show the liquid migrating outwards to the boundary. However, the extent to which this liquid redistribution actually occurs is much smaller than that predicted by the numerical simulation.

The numerical simulation, if allowed to run to large τ, produces ever-increasing values of ϕ at the edges of the domain, which become much larger than the model was designed for. But, even at low porosities which should be within the range being modelled, the simulation predicts much more radial redistribution of fluid than actually occurs. This appears to be a result of the equations themselves, rather than just a numerical error. Another improbable consequence of the equations is that the vertical acceleration is increasing with time. Since the solutions computed here are physically incorrect, it is questionable how much we can use the results to explain even the 'general' observations of fluid moving outward and low-angle bands forming.

6 Conclusions

The model of viscous anisotropy which was employed in this study of pipe Poiseulle flow predicts growth of porosity at the wall of the pipe, and development of high-porosity bands at 15–20° to the vertical. While these qualitative features are both reported experimentally, the quantitative predictions of the model are very different to physical observations. Given this, it can not yet be determined whether an anisotropic viscosity is the correct explanation for the qualitative results.

Clearly some modification is needed in the equations or model. This may mean changes to:

(i) the stress-strain relationship — this could be a change to the form of the viscosity tensor (c_{ijkl}), or a new, non-linear relationship;

(ii) the form of the function $K(\phi)$;

(iii) the assumption of constant r_ξ (in general it could depend on ϕ).

Various alternative stress-strain relationships have been proposed, but none of them yet has been able to fully match the experimental observations.

Despite the need for alterations to the anisotropic viscosity model considered in these notes, our work does suggest that an anisotropic viscosity remains one possibility. A viscosity of this type could play a part in determining the redistribution of porosity and the growth of perturbations at low angles to the vertical. More work will need to be done, and the various models developed some more, before the system can really be understood.

References

A. Baricz. *Generalized Bessel Functions of the First Kind*. Springer, 2010.

S. Butler. Numerical models of shear-induced melt band formation with anisotropic matrix viscosity. *Physics of the Earth and Planetary Interiors*, 200–201:28–36, 2012.

M. Daines and D. Kohlstedt. Influence of deformation on melt topology in periodites. *Journal of Geophysical Research*, 102:10257–10271, 1997.

D.McKenzie. Some remarks on the movement of small melt fractions in the mantle. *Earth and Planetary Science Letters*, 95:53–72, 1989.

T. Driscoll, F. Bornemann, and L. Trefethen. The chebop system for automatic solution of differential equations. *BIT Numerical Mathematics*, 48:701–723, 2008.

U. Faul. Permeability of partially molten upper mantle rocks from experiments and percolation theory. *Journal of Geophysical Research*, 102:10299–10311, 1997.

B. Holtzman, N. Groebner, M. Zimmerman, S. Ginsberg, and D. Kohlstedt. Stress-driven melt segregation in partially molten rocks. *Geochemistry Geophysics Geosystems*, 4, 2003.

R. Katz and M. Spiegelman. An introduction to coupled magma/mantle dynamics. http://foalab.earth.ox.ac.uk/files/IntroMagmaLectures.pdf, 2012. (Online, accessed 10 September 2013).

R. Katz and Y. Takei. Consequences of viscous anisotropy in a deforming, two-phase aggregate: 1. governing equations and linearised analysis. *Journal of Fluid Mechanics*, still to be published, 2013a.

R. Katz and Y. Takei. Consequences of viscous anisotropy in a deforming, two-phase aggregate: 2. numerical solutions of the full equations. *Journal of Fluid Mechanics*, still to be published, 2013b.

R. Katz, M. Knepley, B. Smith, M. Spiegelman, and E. Coon. Numerical simulation of geodynamic processes with the portable extensible toolkit for scientific computation. *Physics of the Earth and Planetary Interiors*, 163:52–68, 2007.

D. King, M. Zimmerman, and D. Kohlstedt. Stress-driven melt segregation in partially molten olivine-rich rocks deformed in torsion. *Journal of Petrology*, 51:21–42, 2010.

D. McKenzie. The generation and compaction of partially molten rock. *Journal of Petrology*, 25:713–765, 1984.

G. Riley and D. Kohlstedt. Kinetics of melt migration in upper mantle-type rocks. *Earth and Planetary Science Letters*, 105:500–521, 1991.

J. Rudge, D. Bercovici, and M. Spiegelman. Disequilibrium melting of a two phase multicomponent mantle. *Geophysical Journal International*, 184:699–718, 2010.

Y. Takei and B. Holtzman. Viscous constitutive relations of solid-liquid composites in terms of grain boundary contiguity: 1. grain boundary diffusion control model. *Journal of Geophysical Research*, 114, 2009a.

Y. Takei and B. Holtzman. Viscous constitutive relations of solid-liquid composites in terms of grain boundary contiguity: 2. compositional model for small melt fractions. *Journal of Geophysical Research*, 114, 2009b.

Y. Takei and B. Holtzman. Viscous constitutive relations of solid-liquid composites in terms of grain boundary contiguity: 3. causes and consequences of viscous anisotropy. *Journal of Geophysical Research*, 114, 2009c.

L. Trefethen. *Approximation Theory and Approximation Practice*. SIAM, 2013.

L. Trefethen and T. A. Driscoll. http://www2.maths.ox.ac.uk/chebfun/guide/, 2011. (Online, accessed 06 September 2013).

D. Wark and E. Watson. Grain-scale permeabilities of texturally equilibrated, monomineralic rocks. *Earth and Planetary Science Letters*, 164:591–605, 1998.

M. Zimmerman, S. Zhang, D. Kohlstedt, and S. Karato. Melt distribution in mantle rocks deformed in shear. *Geophysical Research Letters*, 26, 1999.